

Stochastic Deep Learning Surrogate Models for Uncertainty Propagation in Microstructure-Properties of Ceramic Aerogels

Md Azharul Islam^a, Dwyer Deighan^b, Shayan Bhattacharjee^a, Daniel Tantalo^a,
Pratyush Kumar Singh^a, David Salac^a, Danial Faghihi^{a,*}

^a*Department of Mechanical and Aerospace Engineering,
University at Buffalo, Buffalo, NY, USA*
^b*Computational and Data-Enabled Sciences,
University at Buffalo, Buffalo, NY, USA*

Abstract

Deep learning surrogate models have become pivotal in enabling model-driven materials discovery to achieve exceptional properties. However, ensuring the accuracy and reliability of predictions from these models, trained on limited and sparse material datasets remains a significant challenge. This study introduces an integrated deep learning framework for predicting the synthesis, microstructure, and mechanical properties of ceramic aerogels, leveraging physics-based models such as Lattice Boltzmann simulations for microstructure formation and stochastic finite element methods for mechanical property calculations. To address the computational demands of repeated physics-based simulations required for experimental calibration and material design, a linked surrogate model is developed, leveraging Convolutional Neural Networks (CNNs) for stochastic microstructure generation and microstructure-to-mechanical property mapping. To overcome challenges associated with limited training datasets from expensive physical modeling, CNN training is formulated within a Bayesian inference framework, enabling robust uncertainty quantification in predictions. Numerical results highlight the strengths and limitations of the linked surrogate framework, demonstrating its effectiveness in predicting properties of aerogels with pore sizes and morphologies similar to the training data (in-distribution) and its ability to interpolate to new microstructural features between training data (out-of-distribution).

Keywords: Bayesian inference, convolutional neural networks, surrogate modeling, uncertainty quantification, ceramic aerogel

1. Introduction

Ceramic aerogels, composed of interconnected amorphous ceramic nanoparticles, exhibit a highly porous structure and exceptional thermal insulation properties, making

*Corresponding Author, danialfa@buffalo.edu (D. Faghihi)

them ideal for advanced thermal management in extreme environments. Their applications span civil and military aviation [1], space exploration [2], fire-resistant wearables [3], microelectronics [4, 5], and energy-efficient building systems [6, 7]. However, widespread adoption is hindered by their low mechanical stability. Overcoming this requires model-driven materials discovery [8, 9, 10] to predict synthesis-microstructure-property relationships for optimizing synthesis parameters to create mechanically robust aerogels without compromising insulation performance.

Addressing computational challenges in uncertainty quantification, inference, and optimization for model-driven materials discovery hinges on developing surrogate models that approximate synthesis-to-property relationships. Trained on high-fidelity data, these models enable faster and more efficient predictions. Convolutional Neural Networks (CNNs) have become prominent in computational materials science [11, 12, 13, 14, 15], in generating realistic microstructural images and predicting macroscopic properties. However, their deployment in high-consequence applications, such as materials discovery, faces challenges, including sparse, limited, and stochastic training datasets from physical simulations. Traditional training methods relying on maximum likelihood estimation are prone to overfitting, producing overconfident and unreliable predictions. Furthermore, current approaches for ensuring CNN reliability depend on large datasets, limiting their effectiveness in small-data regimes. Framing training as a Bayesian inference problem offers a robust solution to handling small and uncertain datasets in deep learning surrogate modeling for physical simulations [16, 17]. This approach represents parameter uncertainty through probability distributions, reducing overfitting and enabling uncertainty quantification [18, 19]. However, applying Bayesian inference to CNNs is computationally challenging due to the large number of weight parameters. Zhu et al. [20] addressed this by employing a variational gradient descent algorithm based on Stein’s method, extending Bayesian inference to convolutional encoder-decoder networks. Their approach captured uncertainty in flow through heterogeneous media, even in scenarios where the input (permeability) and output (flow and pressure) fields lacked shared underlying structures. Similarly, Shridhar et al. [21] applied variational inference to estimate posterior weight distributions in CNNs, effectively propagating uncertainty in classification tasks across datasets like MNIST and CIFAR-100.

This work introduces an integrated modeling framework (Figure 1) for simulating the synthesis, microstructure, and properties of ceramic aerogels with high computational efficiency. Specifically, it focuses on a novel synthesis method utilizing in situ bubble-supported pore formation with foaming agents [22, 3], which addresses the limitations of conventional supercritical drying by preserving the porous structure without collapsing the solid matrix. This synthesis enables ambient-pressure, room-temperature drying, significantly reducing processing time while facilitating scalable and cost-effective production of ceramic aerogels. The synthesis-microstructure physics-based model in Figure 1, relies on Lattice Boltzmann simulations of the foaming process, capturing stochastic bubble nucleation, bubble dynamics, and coalescence to predict microstructure formation. The microstructure-property model employs

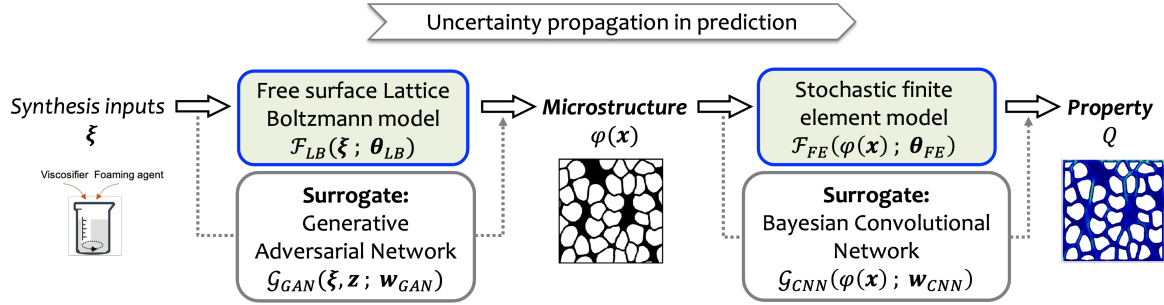


Figure 1: Flowchart of the integrated modeling framework developed in this work for propagating uncertainty through synthesis inputs ξ , microstructure spatial field $\varphi(\mathbf{x})$, and mechanical property Q of ceramic aerogels. The physics-based models, $\mathcal{F}_{LB}(\cdot)$ and $\mathcal{F}_{FE}(\cdot)$, are parameterized by θ_{LB} and θ_{FE} , and utilize synthesis inputs and microstructural patterns to predict material properties. Computational efficiency is achieved through surrogate models $\mathcal{G}_{GAN}(\cdot)$ and $\mathcal{G}_{CNN}(\cdot)$, constructed using high-fidelity training data from physical simulations. The parameter of the surrogate models include the stochastic latent vector \mathbf{z} , deterministic weights of the generative network \mathbf{w}_{GAN} , and posterior probability distributions of the wights \mathbf{w}_{CNN} from the Bayesian inference.

stochastic finite element simulations to analyze the elastic deformation of the solid phase of the aerogel. Using the microstructural patterns, this model computes the displacement and strain fields to estimate the mechanical properties of the aerogel, i.e., the strain energy as the quantity of interest (QoI) for the modeling framework. To enable efficient simulations of synthesis, microstructure, and properties, we develop *linked surrogates* that demonstrate superior representations of the coupled system compared to composite surrogate models directly mapping synthesis inputs to QoI [23]. The microstructure surrogate leverages a scalable generative network trained on microscopic images, enabling the generation of morphologically consistent microstructures across larger domains necessary for macroscopic property predictions. Additionally, the surrogate model of the material property employs a CNN to map microstructural images to the QoI. A key innovation of this framework is the formulation of CNN training as Bayesian inference, enabling the estimation of the probability distribution of weight parameters using high-fidelity training data. To address the computational challenges of Bayesian inference in high-dimensional parameter spaces, we extend the Variational Inference approach used in Bayesian Neural Networks to accommodate the complexity of CNN architectures. The resulting Bayesian Convolutional Neural Network (BayesCNN) mitigates overconfidence in parameter estimation, supports training on small and uncertain datasets derived from high-fidelity simulations, and quantifies the uncertainty in surrogate model predictions. The linked surrogates are systematically employed to characterize and propagate various sources of uncertainty through the synthesis-microstructure-property relationship and the computational prediction of the QoI. This includes capturing microstructural randomness and quantifying errors introduced during surrogate model construction.

The remainder of this manuscript is structured as follows. Section 2 provides an overview of the ceramic aerogel synthesis process, including its modeling using Lat-

tice Boltzmann simulations and the development of surrogate models to represent microstructural patterns. Section 3 describes the stochastic finite element model used to establish microstructure-property relationships and presents the comprehensive formulation and efficient solution algorithm of BayesCNN for surrogate modeling. Section 4 outlines the construction of individual surrogate models, detailing the creation of training datasets from high-fidelity simulations and the validation of these models. Additionally, this section demonstrates the application of the linked-surrogates for propagating of uncertainty from synthesis parameters and stochastic microstructure to the QoI. Finally, Section 5 presents a discussion of the findings and the concluding remarks.

2. Physical and surrogate models of aerogel microstructure

The exceptional thermal insulation of silica aerogels arises from their high porosity and nanoscale pore structure, which limits gas molecule movement. However, widespread use in engineering applications is hindered by the high production costs of current methods, such as supercritical or freeze-drying, e.g., [24]. To overcome these limitations, a novel synthesis process has been developed, utilizing in-situ bubble-supported pore formation for ambient pressure, room-temperature drying [22, 3, 25]. This method employs a silica precursor solution with cetrimonium bromide (CTAB) and an aqueous urea-based foaming agent. Hydrolysis of tetraethyl orthosilicate (TEOS) at CTAB micelle interfaces, combined with urea decomposition and ammonia and carbon dioxide release, generates in-situ bubbles, producing aerogels with randomly distributed pore sizes and morphologies. The primary synthesis inputs ξ include the concentration of TEOS (C_{TEOS}), which regulates the solid phase volume fraction and thereby affects the porosity and pore size of the aerogel. The concentration of CTAB (C_{CTAB}) plays a critical role in bubble formation, influencing the resulting pore size distribution. The concentration of urea (C_{urea}), acting as a foaming agent, reduces surface tension between the precursor solution and gaseous bubbles, thereby impacting the pore distribution. Additionally, the concentration of viscosifier (C_{vis}) determines the stability and morphology of the pore structure during the foaming process. These parameters collectively control the microstructural characteristics and properties of the ceramic aerogel.

2.1. Lattice Boltzmann simulation of microstructure formation

The computational modeling of the ceramic aerogel synthesis process, as discussed in the previous section, requires the integration of key physical phenomena involved in pre-aerogel foaming. These include bubble nucleation, gas diffusion into bubbles, bubble dynamics and coalescence, and the rheological behavior of the precursor, which often exhibits non-Newtonian characteristics. In this study, we utilize the Free Surface Lattice Boltzmann Method (FSLBM) for foaming simulations, e.g., [26, 27, 28, 29]. Specifically, we employ the open-source software package LBfoam [30], which is implemented using the Parallel Lattice Boltzmann (Palabos) library [31] for fluid dynamics

and integrates a Volume-of-Fluid technique for accurate interface tracking. A brief overview of the fundamental equations is provided here for context, while detailed equations and solution algorithms can be found in [30].

The core of FSLBM is the Lattice Boltzmann simulation of complex fluid systems, e.g., [32, 33]. the computational domain is discretized into a regular lattice, where the particle distribution function $f_i(\mathbf{x}, t)$ represents the expected number of particles at lattice site \mathbf{x} and time t in the state $i = 0, 1, \dots, N$ defined by a set of discrete velocities \mathbf{v}_i . The discretized Lattice Boltzmann equation is

$$f_i(\mathbf{x} + \mathbf{v}_i \Delta t, t + \Delta t) = f_i(\mathbf{x}, t) + B(\mathbf{x}, t), \quad (1)$$

with the Bhatnagar-Gross-Krook (BGK) collision operator [33] as,

$$B(\mathbf{x}, t) = -\frac{\Delta t}{\tau} (f_i(\mathbf{x}, t) - f_i^{eq}(\mathbf{x}, t)), \quad (2)$$

where Δt is the time step, τ is a relaxation time, and f_i^{eq} is the distribution function at equilibrium [33]. The solution of Eq. (1) involves two iterative steps: streaming, where the distribution functions f_i move to neighboring lattice sites, and collision, where f_i is locally updated at each site. Macroscopic fluid properties, such as density and velocity, are then derived from the moments of f_i . Building on this foundation, FSLBM simulations utilize a fast mass-tracking algorithm [27] to monitor the interfaces between gas and liquid phases throughout the computational domain. The liquid-gas interface is modeled as a free surface, with the VOF method employed to track the interface using a level function, which represents the liquid fraction within each computational cell. Surface tension σ_{LB} are incorporated by calculating the interface curvature from the level function and applying the resulting pressure jump across the interface. In this work, to capture the highly viscous and shear-thinning behavior of the aerogel precursor, governed by the concentration of viscosifier C_{vis} , the Carreau-Yasuda model [34] is adopted to describe the fluid's rheological properties. The model provides an accurate representation of the non-Newtonian characteristics essential for simulating the foaming process. The influence of TEOS concentration on bubble growth is incorporated by modeling gas diffusion into the bubbles and within the liquid phase using the advection-diffusion equation for gas concentration C ,

$$\frac{\partial C}{\partial t} + \mathbf{v} \cdot \nabla C = D \nabla^2 C + S, \quad (3)$$

where ∇ represents the spatial gradient operator, D denotes the diffusion coefficient, directly linked to C_{TEOS} , and S is a source term representing gas generation or absorption as a function of C_{urea} , which regulates the rate of bubble growth.

Figure 2 presents snapshots of pre-aerogel foaming simulations conducted using FSLBM, illustrating the effects of varying foaming agent concentrations on the resulting ceramic aerogel microstructures. The simulations were initialized with a fluid pool of

height $400 \mu m$, with bubbles of three distinct nuclei sizes ($8 \mu m$, $18 \mu m$, and $25 \mu m$) distributed within the simulation domain using a Poisson disk-sampling algorithm [35]. For all simulations, the fluid density was set to $1 kg/\mu m^3$, ambient pressure to $0.33 N/\mu m^2$, surface tension to $\sigma_{LB} = 5 \times 10^{-3} N/\mu m$, and the advection-diffusion source term to $S = 5 \times 10^{-5} \mu m^2/s$. The variation in the number of initial bubbles and their radii led to distinct classes of ceramic microstructures with different average pore size at the final simulation time. As demonstrated later, the use of the Poisson disk-sampling algorithm enables FSLBM to generate multiple ensemble realizations for each microstructure class with the same numbers and initial radius of the bubbles to account for stochasticity of the aerogel microstructure.

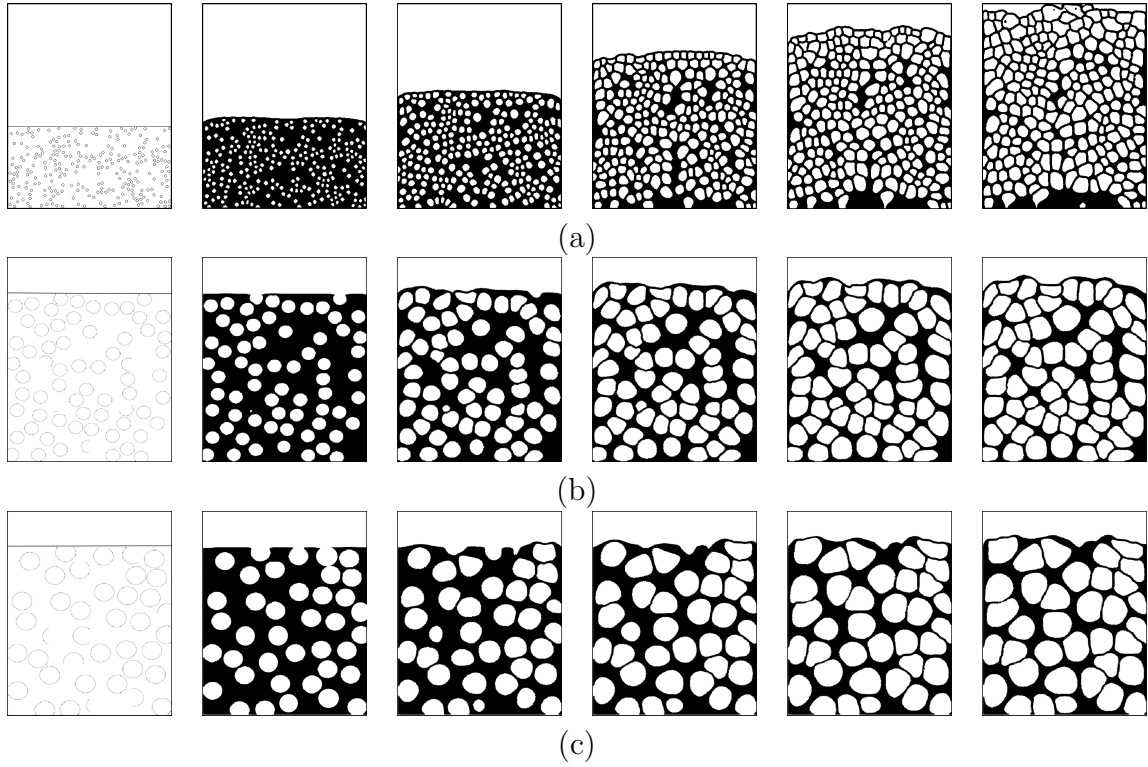


Figure 2: FSLBM simulations of the ceramic aerogel foaming process (pores in white) showing the time evolution of bubbles' growth and coalescence in the pre-aerogel to form a porous microstructure. All simulations are conducted over 20 minutes and 5000 timesteps each with $\Delta t = 2s$ and all the physical parameters are kept unchanged except the initial number of bubbles n_{bub} and initial bubble radius r_{bub} leading to different average aerogel pore size at the end of simulation: (a) $n_{bub} = 250$, $r_{bub} = 8$, leading to pore radius $8\mu m$; (b) $n_{bub} = 50$, $r_{bub} = 18$, leading to pore radius $18\mu m$; (c) $n_{bub} = 25$, $r_{bub} = 25$, leading to pore radius $25\mu m$. The simulation domain height was $550 \mu m$ and width was $400 \mu m$, with $400 \mu m$ fluid pool height throughout the simulations.

2.2. Generative surrogate model of aerogel microstructure

FSLBM simulations of aerogel microstructures are computationally intensive, making tasks such as uncertainty quantification, requiring numerous evaluations of $\mathcal{F}_{LB}(\xi; \theta_{LB})$ prohibitively expensive. To enable computationally efficient synthesis-microstructure

mapping, we propose a surrogate model for FSLBM simulations based on the Generative Adversarial Network (GAN) introduced by [36]. GANs employ two deep convolutional neural networks: the generator $\mathcal{G}_{GAN}(\cdot)$ and the discriminator $\mathcal{D}(\cdot)$. These networks are trained an adversarial manner in a two-player minimax game, where the generator, parameterized by \mathbf{w}_{GAN} , maps a random latent input vector to the data space p_G , approximating the real data distribution p_{data} . Meanwhile, the discriminator, with weight parameters \mathbf{w}_{dis} , acts as a classifier, outputting the probability of a sample being real or generated. In this unsupervised learning setup, the generator minimizes the divergence between p_G and p_{data} , while the discriminator maximizes it, until both networks reach a Nash equilibrium. Once trained on microstructural imaging data, the generator can efficiently produce ensembles of microstructures that closely replicate the characteristics of the training data. In recent years, the application of GANs to imaging and digital material data has gained significant attention, demonstrating their potential in capturing realistic microstructural features, e.g., [37, 38, 39, 40, 41].

To formulate the generative surrogate model for ceramic aerogel microstructures, we define a *microstructure indicator function* $\varphi(\mathbf{x})$, as illustrated in Figure 1. This spatial field assigns values of $\varphi = 0$ to the spatial points \mathbf{x} within the pores and $\varphi = 1$ to those within the solid skeleton of the aerogel. The objective of the surrogate model is to generate a large ensemble of aerogel microstructural patterns, such that

$$\varphi(\mathbf{x}) = \mathcal{G}_{GAN}(\boldsymbol{\xi}, \mathbf{z}; \mathbf{w}_{GAN}), \quad (4)$$

where $\mathcal{G}_{GAN}(\boldsymbol{\xi}, \mathbf{z}; \mathbf{w}_{GAN})$ is the GAN’s generator, a fully convolutional neural network parameterized by weight vector \mathbf{w}_{GAN} that up-convolve the random vector of *latent variable* $\mathbf{z} \sim p_z(\mathbf{z})$ where p_z is a Gaussian zero mean distribution, scaling its dimension up at each layer, to produce microstructure image. A key feature of (4) is that the generator is conditioned on the synthesis inputs $\boldsymbol{\xi}$ as an additional input. During training, \mathbf{z} varies randomly, while $\boldsymbol{\xi}$ are set to the corresponding synthesis input used to generate the training data, which consist of microstructural images obtained from FSLBM simulations. Once trained, $\mathcal{G}_{GAN}(\boldsymbol{\xi}, \mathbf{z}; \mathbf{w}_{GAN})$ can efficiently generate random microstructure patterns $\varphi(\mathbf{x})$ by sampling \mathbf{z} while by varying $\boldsymbol{\xi}$, the model can produce a wide range of diverse and novel morphologies that correspond to different aerogel synthesis conditions, including those interpolated between training data points.

Training vanilla GANs is notoriously challenging, often requiring significant manual intervention to stabilize the training process. To address these challenges, we utilize Wasserstein GANs with Gradient Penalty (WGAN-GP), as proposed by [42]. WGAN-GP enhances stability by imposing Lipschitz continuity constraints on the discriminator and introducing a gradient penalty term into the discriminator’s loss function. Like vanilla GANs, WGAN-GP is formulated as a two-player zero-sum game, expressed as:

$$\inf_{\mathbf{w}_{GAN}} \sup_{\substack{\mathbf{w}_{dis} \\ \mathcal{D} \text{ is 1-Lipschitz}}} \mathbb{E}_{\varphi(\mathbf{x}) \sim p_{data}} [\mathcal{D}(\varphi(\mathbf{x}); \mathbf{w}_{dis})] - \mathbb{E}_{\mathbf{z} \sim p_z(\mathbf{z})} [\mathcal{D}(\mathcal{G}(\varphi(\mathbf{x}); \mathbf{w}_{GAN}); \mathbf{w}_{dis})]. \quad (5)$$

The loss functions for the generator and discriminator in the WGAN-GP are defined as,

$$\mathcal{L}_g = -\mathbb{E}_{\mathbf{z} \sim p_z(\mathbf{z})} [\mathcal{D}(\mathcal{G}(\boldsymbol{\xi}, \mathbf{z}; \mathbf{w}_{GAN}); \mathbf{w}_{dis})] \quad (6)$$

$$\begin{aligned} \mathcal{L}_d &= \mathbb{E}_{\mathbf{z} \sim p_z(\mathbf{z})} [\mathcal{D}(\mathcal{G}(\boldsymbol{\xi}, \mathbf{z}; \mathbf{w}_{GAN}); \mathbf{w}_{dis})] - \mathbb{E}_{\varphi(\mathbf{x}) \sim p_{data}} [\mathcal{D}(\varphi(\mathbf{x}); \mathbf{w}_{dis})] \\ &+ c_\lambda \mathbb{E}_{\hat{\varphi}(\mathbf{x}) \sim p_{\hat{\varphi}(\mathbf{x})}} [(\|\nabla_{\hat{\varphi}(\mathbf{x})} \mathcal{D}(\hat{\varphi}(\mathbf{x}); \mathbf{w}_{dis})\|_2 - 1)^2], \end{aligned} \quad (7)$$

where $p_{\hat{\varphi}(\mathbf{x})}$ represents the distribution obtained by uniformly sampling points along straight lines between pairs of samples from p_{data} and p_G . The discriminator's loss consists of three components: the first two terms calculate the Wasserstein-1 distance, measuring the difference between real and generated distributions, while the third term imposes a gradient penalty to enforce Lipschitz continuity, with c_λ as the regularization weight. The generator's loss minimizes the discriminator's evaluation of the generated samples, encouraging the generator to produce more realistic outputs [43].

3. Physical and surrogate models of aerogel mechanical properties

This section introduces a physics-based model for analyzing stress and strain distribution within the two-phase aerogel material. Additionally, it describes the development of a microstructure-property surrogate model using a Bayesian convolutional neural network (BayesCNN). Coupled with the microstructural images generated by the WGAN-GP model outlined in Section 2.2, the linked-surrogates enables facilitates efficient prediction of the quantity of interest (QoI), specifically the strain energy.

3.1. Stochastic finite element model of aerogel elastic deformation

To accurately simulate the interplay between microstructural features and macroscopic mechanical properties of ceramic aerogels, we employ a finite element (FE) model governed by a stochastic partial differential equation. This model determines the displacement and stress fields based on the microstructural images of the aerogel. Let Ω represent a bounded domain in \mathbb{R}^d , where d can be 1, 2, or 3 with Lipschitz boundary, and let the boundary of this domain be denoted by $\partial\Omega$. The goal is to determine the displacement field $\mathbf{u}(\mathbf{x})$ at spatial points $\mathbf{x} \in \Omega$. The governing equation is expressed as:

$$\begin{aligned} \nabla \cdot \mathbf{T}(\mathbf{u}) &= \mathbf{f}(\mathbf{x}), \quad \mathbf{x} \in \Omega, \\ \mathbf{T}(\mathbf{u})\mathbf{n} &= \mathbf{t}(\mathbf{x}), \quad \mathbf{x} \in \Gamma_N, \\ \mathbf{u}(\mathbf{x}) &= \mathbf{u}^*, \quad \mathbf{x} \in \Gamma_D, \end{aligned} \quad (8)$$

where, \mathbf{f} is a prescribed source term, \mathbf{t} is traction, Γ_N is the subset of the boundary $\partial\Omega$ where the Neumann boundary condition is applied, $\Gamma_D = \partial\Omega \setminus \Gamma_N$ represents the boundary subject to Dirichlet conditions. The Cauchy stress tensor \mathbf{T} is defined as:

$$\mathbf{T}(\mathbf{u}) = 2\mu_s \varphi(\mathbf{x}) \mathbf{E}(\mathbf{u}) + \lambda_s \varphi(\mathbf{x}) \text{tr}(\mathbf{E}(\mathbf{u}))\mathbf{I}, \quad (9)$$

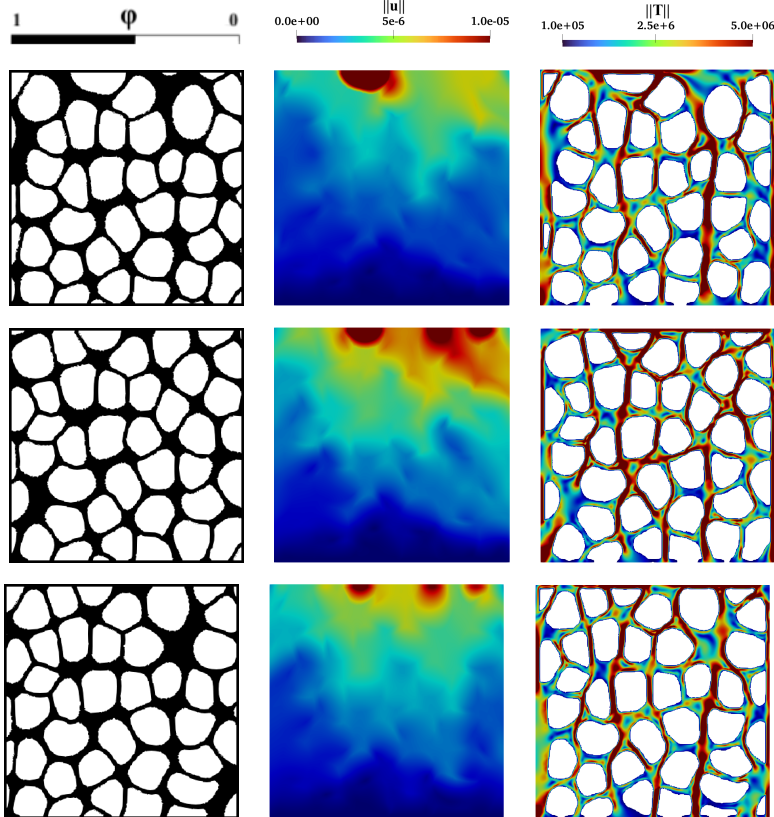


Figure 3: Finite element (FE) simulation results for three microstructure indicator functions, showing the magnitude of displacement and Cauchy stress fields. For the FE simulations, young’s modulus for solid $E_s = 100 \times 10^6$ Pa, poisson’s ratio $\nu = 0.3$ was used. A traction force of 10^6 N was applied in the negative y direction (compression).

where, λ_s and μ_s are the Lamé constants of the solid aerogel phase, equivalent to the material’s Young’s modulus E_s and Poisson’s ratio ν_s , $\mathbf{E}(\mathbf{u}) = \frac{1}{2} (\nabla \mathbf{u} + (\nabla \mathbf{u})^T)$ is the strain tensor, and $\varphi(\mathbf{x})$ is the stochastic microstructure indicator function generated by the WGAN-GP surrogate model described in the previous section. Figure 3 illustrates the displacement and stress fields computed for a single realization of three different microstructure classes. The governing equation in (8) is solved using a uniformly fine mesh to resolve the intricate microstructural patterns represented by $\varphi(\mathbf{x})$. The FEM implementation is performed using the DOLFINx library [44] from the FEniCS Project in Python. The prediction QoI is the scalar strain energy, computed as:

$$Q = \int_{\Omega} \mathbf{T}(\mathbf{u}) : \mathbf{E}(\mathbf{u}) dx. \quad (10)$$

3.2. Bayesian convolutional neural network surrogate model

To develop a surrogate model linking microstructure to mechanical properties, we employ a Bayesian convolutional neural network (CNN) that maps a microstructure image of ceramic aerogel $\varphi(\mathbf{x})$ to the corresponding strain energy output $Q^{CNN} = \mathcal{G}_{CNN}(\varphi_i; \mathbf{w}_{CNN})$ (see Figure 1). This mapping is parameterized by the weights \mathbf{w}_{CNN}

of the filters of the convolutional layers and the fully-connected layers of the CNN architecture, which are determined through training. The training dataset, denoted as $\mathbf{D} = \{(\varphi_i, Q_i^{FE})\}_{i=1}^{N_D}$ consists of N_D samples furnished by the stochastic finite element model described in previous section, such that $Q_i^{FE} = \mathcal{F}_{FE}(\varphi_i; \boldsymbol{\theta}_{FE})$. Traditional CNN training rely on maximum likelihood estimation of the weight parameters to minimize the error between the output and the training data. However, these approaches fail to explicitly account for the uncertainty in CNN weight parameters that translate to uncertainty in the output, which becomes critical in scenarios involving small and uncertain datasets. In contrast, a Bayesian framework provides a more robust approach by inferring probability distribution of the weights from data using the Bayes' rule,

$$\pi_{\text{post}}(\mathbf{w}_{CNN} | \mathbf{D}) = \frac{\pi_{\text{like}}(\mathbf{D} | \mathbf{w}_{CNN})\pi_{\text{prior}}(\mathbf{w}_{CNN})}{\pi_{\text{evid}}(\mathbf{D})}, \quad (11)$$

where $\pi_{\text{prior}}(\mathbf{w}_{CNN})$ is prior distribution of the weights, $\pi_{\text{like}}(\mathbf{D} | \mathbf{w}_{CNN})$ is the likelihood of observing the data given the weights, and $\pi_{\text{evid}}(\mathbf{D})$ is the evidence, a normalization factor ensuring that the posterior integrates to 1. The posterior distribution $\pi_{\text{post}}(\mathbf{w}_{CNN} | \mathbf{D})$ reflects the updated knowledge of the weights after incorporating the training data. Given this posterior distribution, for any new microstructure $\varphi^*(\mathbf{x})$ the strain energy output can be predicted using the predictive distribution,

$$\pi(Q^{CNN*} | \varphi^*, \mathbf{D}) = \int \pi(Q^{CNN*} | \varphi^*, \mathbf{w}_{CNN}) \pi_{\text{post}}(\mathbf{w}_{CNN} | \mathbf{D}) d\mathbf{w}_{CNN}. \quad (12)$$

In practice, a collection of M_{mc} samples are drawn from posterior $\hat{\mathbf{w}}_{CNN}^{(j)} \sim \pi_{\text{post}}(\mathbf{w}_{CNN} | \mathbf{D})$ and the prediction distribution can then be approximated using Monte Carlo estimation, which is expressed as:

$$\begin{aligned} \pi(Q^{CNN*} | \varphi^*, \mathbf{D}) &= \mathbb{E}_{\mathbf{w}_{CNN} | \mathbf{D}} [\pi(Q^{CNN*} | \varphi^*, \mathbf{w}_{CNN})] \\ &\approx \frac{1}{M_{mc}} \sum_{j=1}^{M_{mc}} \mathcal{G}_{CNN}(\varphi^*; \hat{\mathbf{w}}_{CNN}^{(j)}). \end{aligned} \quad (13)$$

Variational Inference. To achieve computationally efficient Bayesian inference for high-dimensional parameter spaces, we employ variational inference, an optimization-based technique that approximates the true posterior distribution $\pi_{\text{post}}(\mathbf{w}_{CNN} | \mathbf{D})$ with a tractable variational distribution $q_{\boldsymbol{\eta}}(\mathbf{w}_{CNN})$, parameterized by $\boldsymbol{\eta}$ and often chosen from a family of distributions such as Gaussians. The optimal variational distribution q^{opt} is obtained by minimizing the Kullback-Leibler (KL) divergence between the variational distribution and the true posterior,

$$q^{\text{opt}} = \arg \min_q \{ \text{KL} [q_{\boldsymbol{\eta}}(\mathbf{w}_{CNN}) || \pi_{\text{post}}(\mathbf{w}_{CNN} | \mathbf{D})] \}, \quad (14)$$

where the KL divergence is defined as:

$$\begin{aligned} \text{KL}[q_{\boldsymbol{\eta}}(\mathbf{w}_{CNN})||\pi_{\text{post}}(\mathbf{w}_{CNN} | \mathbf{D})] &= \int q_{\boldsymbol{\eta}}(\mathbf{w}_{CNN}) \ln \frac{q_{\boldsymbol{\eta}}(\mathbf{w}_{CNN})}{\pi_{\text{post}}(\mathbf{w}_{CNN} | \mathbf{D})} d\mathbf{w}_{CNN} \\ &= \mathbb{E}_{q_{\boldsymbol{\eta}}} \left[\ln \frac{q_{\boldsymbol{\eta}}(\mathbf{w}_{CNN})}{\pi_{\text{post}}(\mathbf{w}_{CNN} | \mathbf{D})} \right]. \end{aligned} \quad (15)$$

Then, the prediction in (12) is performed with replacing the posterior with the tractable variational approximation q^{opt} . Substituting the posterior from Bayes' theorem (11) into the (15) gives,

$$\begin{aligned} \text{KL}[q_{\boldsymbol{\eta}}(\mathbf{w}_{CNN})||\pi_{\text{post}}(\mathbf{w}_{CNN} | \mathbf{D})] &= - \mathbb{E}_{q_{\boldsymbol{\eta}}} \left[\ln \frac{\pi_{\text{prior}}(\mathbf{w}_{CNN})}{q_{\boldsymbol{\eta}}(\mathbf{w}_{CNN})} \right] \\ &\quad - \mathbb{E}_{q_{\boldsymbol{\eta}}} [\ln \pi_{\text{like}}(\mathbf{D} | \mathbf{w}_{CNN})] \\ &\quad + \mathbb{E}_{q_{\boldsymbol{\eta}}} [\ln \pi_{\text{evid}}(\mathbf{D})]. \end{aligned} \quad (16)$$

The evidence $\pi_{\text{evid}}(\mathbf{D})$ is independent of the variational distribution $q_{\boldsymbol{\eta}}(\mathbf{w}_{CNN})$, so the last term in the above equation $\mathbb{E}_{q_{\boldsymbol{\eta}}} [\ln \pi_{\text{evid}}(\mathbf{D})] = \ln \pi_{\text{evid}}(\mathbf{D})$ and does not contribute to the minimization problem in (14). This leads to the definition of the evidence lower bound (ELBO),

$$\begin{aligned} L[q_{\boldsymbol{\eta}}(\mathbf{w}_{CNN})] &= \mathbb{E}_{q_{\boldsymbol{\eta}}} \left[\ln \frac{\pi_{\text{prior}}(\mathbf{w}_{CNN})}{q_{\boldsymbol{\eta}}(\mathbf{w}_{CNN})} \right] + \mathbb{E}_{q_{\boldsymbol{\eta}}} [\ln \pi_{\text{like}}(\mathbf{D} | \mathbf{w}_{CNN})] \\ &= -\text{KL}[q_{\boldsymbol{\eta}}(\mathbf{w}_{CNN})||\pi_{\text{prior}}(\mathbf{w}_{CNN})] + \mathbb{E}_{q_{\boldsymbol{\eta}}} [\ln \pi_{\text{like}}(\mathbf{D} | \mathbf{w}_{CNN})]. \end{aligned} \quad (17)$$

Thus, the KL divergence can be rewritten as:

$$\text{KL}[q_{\boldsymbol{\eta}}(\mathbf{w}_{CNN})||\pi_{\text{post}}(\mathbf{w}_{CNN} | \mathbf{D})] = -L[q_{\boldsymbol{\eta}}(\mathbf{w}_{CNN})] + \ln \pi_{\text{evid}}(\mathbf{D}), \quad (18)$$

where minimizing the KL divergence is equivalent to maximizing $L[q_{\boldsymbol{\eta}}(\mathbf{w}_{CNN})]$ over $q_{\boldsymbol{\eta}}(\mathbf{w}_{CNN})$ and ELBO provides a lower bound on $\ln \pi_{\text{evid}}(\mathbf{D})$. Considering the additive noise model, assuming Gaussian-distributed total error resulting from data noise and model inadequacy, the log-likelihood function is given by:

$$\ln \pi_{\text{like}}(\mathbf{D} | \mathbf{w}_{CNN}) = -\frac{N_D}{2} \ln(2\pi\sigma_{\text{noise}}) - \frac{1}{2\sigma_{\text{noise}}} \sum_{i=1}^{N_D} (Q_i^{CNN} - Q_i^{FE})^2. \quad (19)$$

where $R(\mathbf{w}_{CNN}) = \sum_{i=1}^{N_D} (Q_i^{CNN} - Q_i^{FE})^2$ is called the data misfit and σ_{noise} is the noise variance, a hyperparameter that balances the influence of the prior (regularization term) and likelihood (data misfit term) in computing the posterior distribution. The

expectation of the log-likelihood is evaluated using Monte Carlo sampling,

$$\mathbb{E}_{q_{\boldsymbol{\eta}}(\mathbf{w}_{CNN})}[\ln \pi_{\text{like}}(\mathbf{D} \mid \mathbf{w}_{CNN})] = \frac{1}{M_{mc}} \sum_{j=1}^{M_{mc}} \ln \pi_{\text{like}}(\mathbf{D} \mid \hat{\mathbf{w}}_{CNN}^{(j)}), \quad (20)$$

where $\hat{\mathbf{w}}_{CNN}^{(j)} \sim q_{\boldsymbol{\eta}}(\mathbf{w}_{CNN})$ are samples drawn from the variational distribution, and M_{mc} is the number of samples. In practice, the variational distribution is expressed as a product of independent Gaussian distributions following the mean-field approximation,

$$q_{\boldsymbol{\eta}}(\mathbf{w}_{CNN}) = \prod_{i=1}^s \mathcal{N}(w_{CNN_i}; \mu_i, \sigma_i), \quad (21)$$

where the variational parameters $\boldsymbol{\eta}$ consist of the means and standard deviations of each Gaussian component, $\boldsymbol{\eta} = \{\mu_i, \sigma_i\}_{i=1}^d$. Bayesian inference is then framed as optimizing the variational parameters $\boldsymbol{\eta}$ to ensure that the variational density closely approximates the true posterior distribution. Using the ELBO from (23), this can be written as,

$$\boldsymbol{\eta}^{\text{opt}} = \arg \min_{\boldsymbol{\eta}} \left\{ \text{KL} [q_{\boldsymbol{\eta}}(\mathbf{w}_{CNN}) \parallel \pi_{\text{prior}}(\mathbf{w}_{CNN})] - \mathbb{E}_{q_{\boldsymbol{\eta}}} [\ln \pi_{\text{like}}(\mathbf{D} \mid \mathbf{w}_{CNN})] \right\}. \quad (22)$$

Considering Gaussian prior, the first term in (22) has a closed-form solution, while the second term can be evaluated using (20). For numerical optimization, the ELBO from (17) is reformulated as,

$$\text{L}[q_{\boldsymbol{\eta}}(\mathbf{w}_{CNN})] \propto \beta \text{KL} [q_{\boldsymbol{\eta}}(\mathbf{w}_{CNN}) \parallel \pi_{\text{prior}}(\mathbf{w}_{CNN})] + \frac{1}{M_{mc}} \sum_{j=1}^{M_{mc}} R(\hat{\mathbf{w}}_{CNN}^{(j)}), \quad (23)$$

where $\beta = 2\sigma_{\text{noise}}$ and the right-hand side of the (23) is employed in the optimization process to determine the variational parameters. To enhance the efficiency of gradient-based optimization, we applied the local reparameterization trick to convolutional layers. This approach preserves computational performance while enabling efficient updates of variational parameters. The optimization technique, commonly referred to as ‘‘Bayes by Backprop’’ [17], facilitates the training of BayesCNN by leveraging this reparameterization framework.

4. Numerical results

This section presents computational results from the integrated modeling framework (Figure 1), focusing on the development and evaluation of WGAN-GP and BayesCNN surrogate models. Their predictive accuracy is assessed against high-fidelity methods, including the Free-surface Lattice Boltzmann Method (FSLBM) and stochastic Finite Element (FE) simulations. The linked surrogates are then used to propagate uncertainty through the synthesis-microstructure-property relationships, analyzing the

impact of microstructural randomness and surrogate model errors on the reliability of the predicted quantities of interest (QoI).

4.1. Generative surrogate model of microstructure

We detail the construction of the WGAN-GP surrogate model and quantitatively evaluate its performance by comparing microstructure images and morphological features generated by the WGAN-GP to the ones from FSLBM simulations.

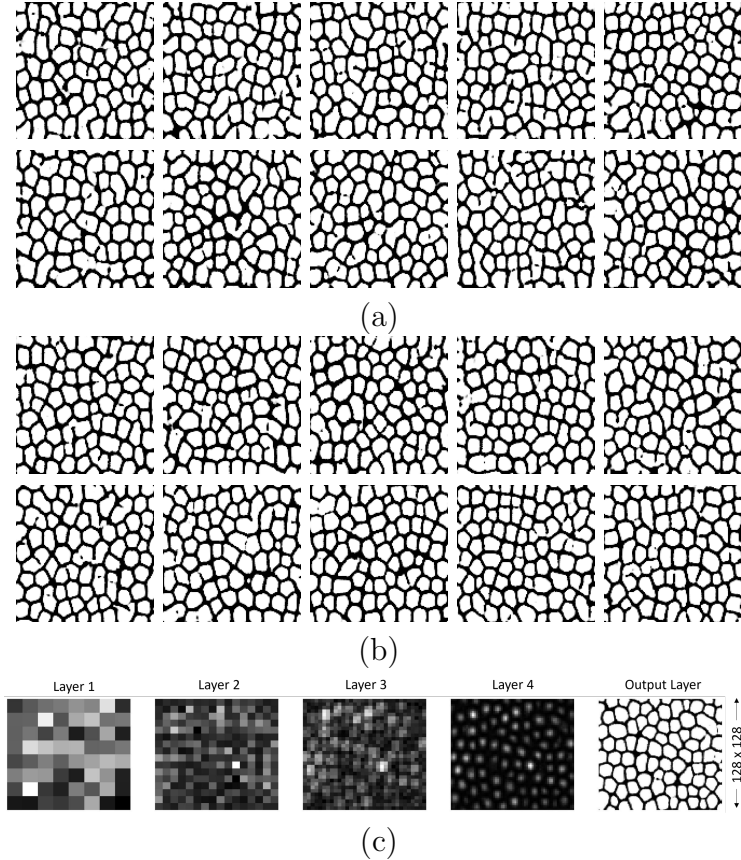


Figure 4: Examples of microstructures of aerogel with average pore radii of $6\mu\text{m}$: (a) Training images obtained from the FSLBM simulations of the foaming process $\mathcal{F}_{LB}(\xi; \theta_{LB})$. (b) Generated images obtained from the WGAN-GP’s generator network after training $\mathcal{G}_{GAN}(\xi, z; \mathbf{w}_{GAN})$. (c) Feature maps of each layer in the generator network.

Networks architecture and training. The WGAN-GP generator network consists of four layers, each with a Convolutional Transpose, Batch Normalization, and ReLU activation, followed by a final layer with a Convolutional Transpose and Tanh activation to output the generated microstructure image. A latent vector z of size 4×1 is progressively upscaled by a factor of 2 in each subsequent layer to produce the $128 \times 128 \times 1$ microstructure. The discriminator network mirrors this structure, using Convolutional, Batch Normalization, and Leaky ReLU layers, with a final Convolutional layer producing a scalar output representing the Wasserstein distance between

synthetic and generated image distributions. Both networks employ a 4×4 kernel, 2×2 stride, and 1×1 padding, achieving a scaling factor of 2^5 ($=32$) over five layers. The architectures, summarized in Table A.1 (see Appendix), are adapted from previous GAN-based material microstructure models [37, 38], with modifications tailored to this study. The training dataset comprises 128×128 pixel microstructure images created using FSLBM simulations, $\mathcal{F}_{LB}(\boldsymbol{\xi}; \boldsymbol{\theta}_{BL})$. The WGAN-GP was trained on 2,500 synthetic images from FSLBM simulations (Figure 2(a)) with an average pore size of $6 \mu m$. Training employed the Adam optimizer with a learning rate of 0.0002, a batch size of 10, and a discriminator penalty coefficient $c_\lambda = 10$, over 2000 epochs.

Accuracy of the generated microstructure images. Figure 4 illustrates a comparison between microstructure images of aerogels from FSLBM simulations and WGAN-GP surrogate model. The accuracy of the WGAN-GP is quantitatively assessed by comparing morphological attributes including pore size distribution and the two-point correlation function. Figure 5(a) shows the Kernel Density Estimate (KDE) of pore diameters for 30 samples, revealing close agreement between data and generated microstructures. Pore diameters were calculated using an image segmentation method that labels individual pores, determines their areas (based on pixel counts), and computes the equivalent diameter of a circle with the same area. Further details on this method are provided in [45]. The two-point correlation function, $S_2(\mathbf{r})$, is a statistical measure

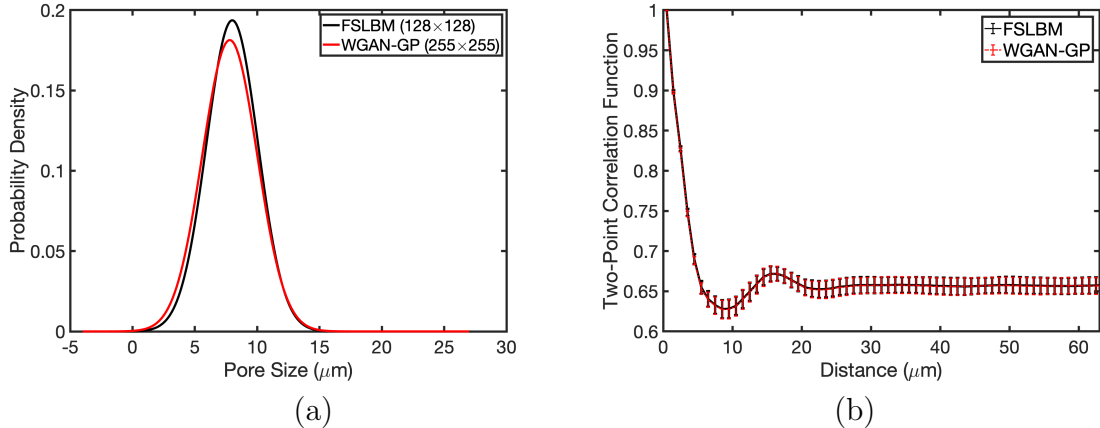


Figure 5: Morphological features of 30 microstructure images obtained from FSLBM simulation and generated by WGAN-GP: (a) Probability distribution of pore diameters. (b) 1D plots of the two-point correlation function.

characterizing the morphology of two-phase media [46], representing the probability that two points separated by $|\mathbf{r}|$ belong to the same phase. Here, we focus on the pore phase (pixels with a value of 255) to quantify pore distribution within a given distance \mathbf{r} . Figure 5(b) shows 1D plots of $S_2(\mathbf{r})$ for 30 synthetic and generated samples, with error bars capturing sample variability. The close agreement demonstrates the WGAN-GP’s ability to reproduce microstructural features consistent with FSLBM simulations.

Scalable microstructure generator. Despite the widespread application of GANs in modeling material microstructures, their utility is fundamentally constrained by the fixed size of training images. However, material properties of practical interest are often required at the component level, involving domains several orders of magnitude larger than those captured by microscale imaging or modeling techniques. To overcome this limitation, we propose a novel approach that enables the generation of arbitrary-sized microstructure images using WGAN-GP trained on smaller image datasets. This method utilizes a latent vector as input to the generator, trained in a low-dimensional latent space, allowing efficient generation of microstructures at various scales while maintaining control over the output dimensions.

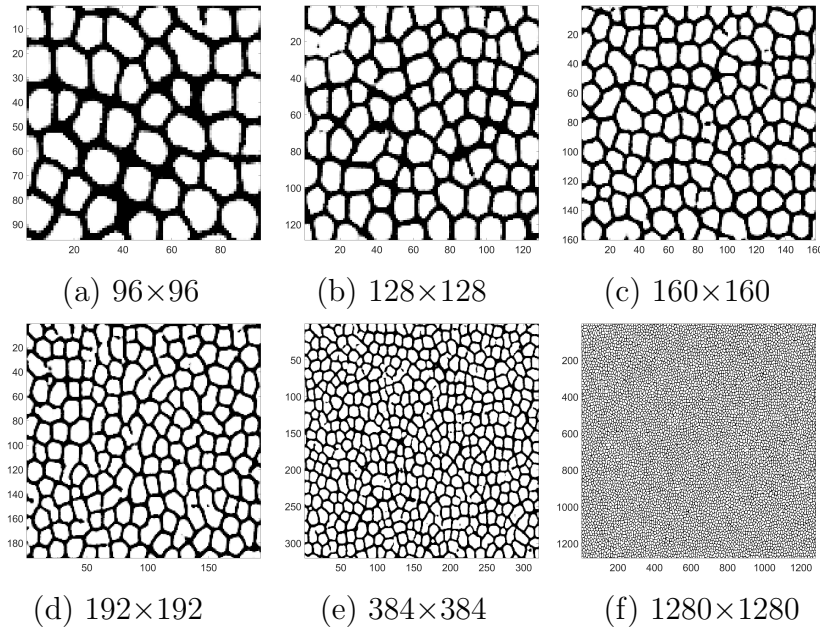


Figure 6: Generated microstructural images of varying dimensions (in pixels) produced by the scalable generator network in WGAN-GP, corresponding to ceramic aerogel domain sizes of (a) $52.5 \mu\text{m}$, (b) $70 \mu\text{m}$, (c) $87.5 \mu\text{m}$, (d) $105 \mu\text{m}$, (e) $210 \mu\text{m}$, and (f) $700 \mu\text{m}$.

As described, the generator architecture, trained with a latent vector \mathbf{z} of size 4×1 , provides an upscaling factor of 2 per layer. However, increasing the image dimensions requires adding more convolutional layers, which also necessitates corresponding layers in the discriminator. This increases network complexity, training time, and computational cost. To address these issues, we reformulate the generator architecture by separating it from the fully connected layers and using linear transformations to reshape the latent vector \mathbf{z} . Specifically, \mathbf{z} of dimension 4×1 is mapped to a latent variable of dimension $(-1, \text{hidden_dim}, 4, 4)$ where `hidden_dim` is the hidden dimension size, and `-1` denotes the arbitrary batch size. This approach provides more flexibility over the size of the latent vector we input to the generator, and this also results in the reduction of the total number of layers. Importantly, this method preserves the microstructural features while allowing for the efficient generation of images at arbitrary

dimensions. Figure 6 shows microstructures of various sizes generated by the scalable WGAN-GP, trained on 128×128 pixel synthetic microstructures (corresponding to a $70 \mu\text{m}$ aerogel domain). The output size is controlled by the dimensions of the latent variable, providing flexibility. Figure 7 compares the KDEs of pore sizes from 30 synthetic microstructures and larger generated images. The agreement highlights the scalable generator’s ability to produce larger microstructure images while preserving key statistical features across different sizes.

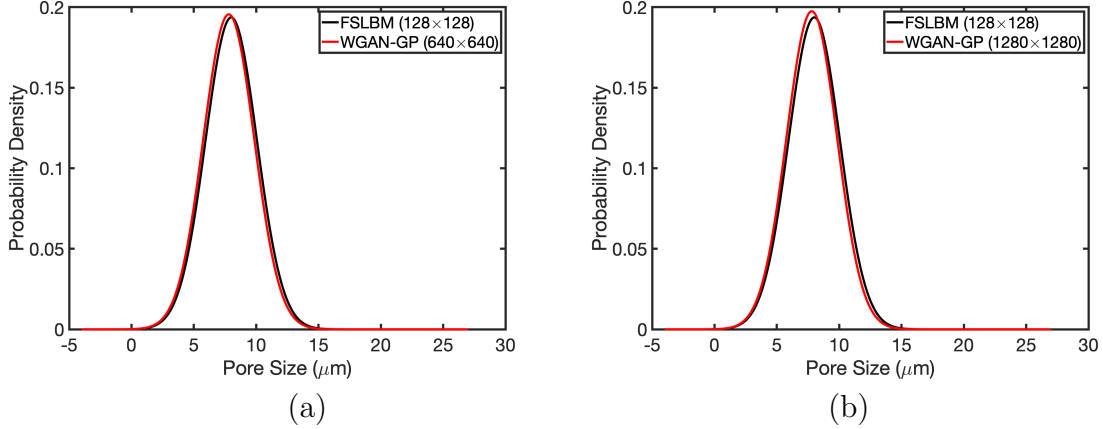


Figure 7: Comparison of pore diameter probability distributions between the 128×128 microstructures obtained from FSLBM simulations and scaled generated microstructures from WGAN-GP with dimensions: (a) 640×640 pixels ($350 \mu\text{m}$), (b) 1280×1280 pixels ($700 \mu\text{m}$).

4.2. BayesCNN surrogate model of mechanical properties

This section describes the construction of the BayesCNN surrogate model, using high-fidelity simulations from the stochastic FE model, to predict the mapping between microstructure images and the strain energy of ceramic aerogels (QoI). The surrogate model’s performance with quantified uncertainty, is validated for both *in-distribution* and *out-of-distribution* predictions. *In-distribution* refers to microstructures with pore sizes and morphology similar to the training data, while *out-of-distribution* includes microstructures with characteristics that interpolate between the training data.

High-fidelity data. Three categories of ceramic aerogel microstructures: *small pores*, *medium pores*, and *large pores*, with average pore sizes of $6\mu\text{m}$, $18\mu\text{m}$, and $25\mu\text{m}$, respectively, is taken into account (Figure 8). A total of 1,188 samples (396 per category) were simulated using the stochastic FE model $\mathcal{F}_{FE}(\varphi, \boldsymbol{\theta}_{FE})$ to compute the strain energy Q^{FE} . For all samples, uniaxial loading conditions are applied with traction of $t_y = -10^6 N$ being imposed downward on the top surface, while the displacement at the bottom boundary of the domain are fixed. The resulting microstructure-strain energy data was randomly divided into 90% training dataset and 10% in-distribution dataset.

Additionally, to assess the BayesCNN’s generalizability, an out-of-distribution dataset was generated using FSLBM simulations. This dataset includes 10 microstructures

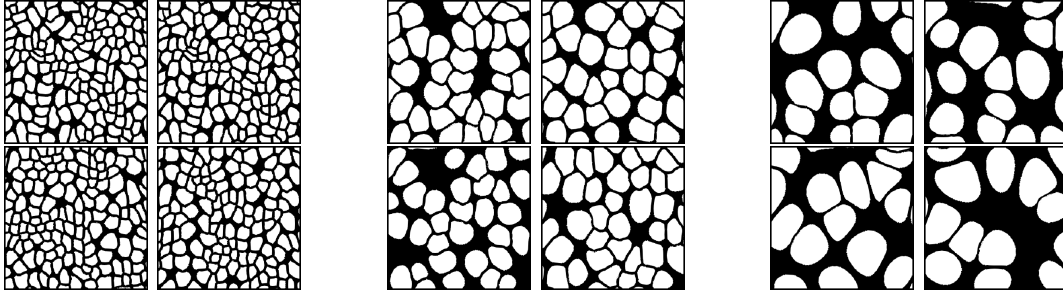
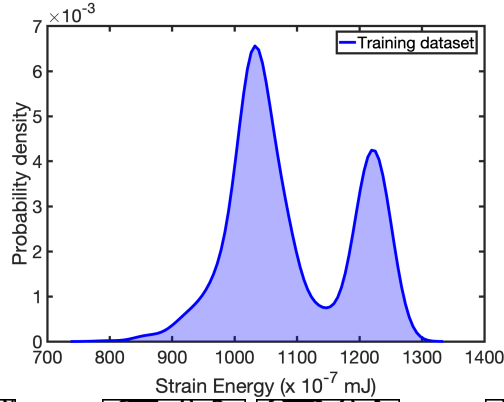
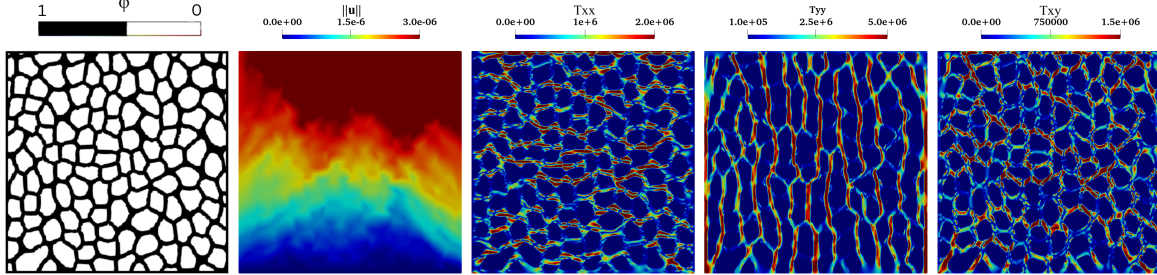
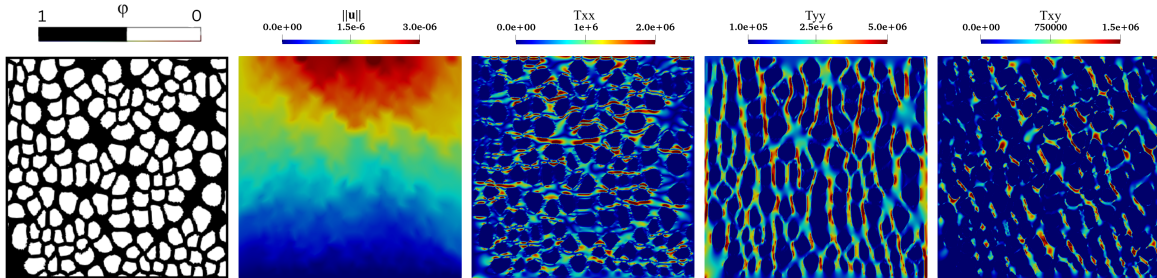


Figure 8: High-fidelity training data to construct the BayesCNN surrogate model. Probability distribution of strain energy Q^{FE} computed using the stochastic FE model $\mathcal{F}_{FE}(\varphi, \theta_{FE})$ and samples of three microstructure categories: *small pores* with average pore sizes of $6\mu\text{m}$; *medium pores* with average pore sizes of $18\mu\text{m}$; *large pores* with average pore sizes of $25\mu\text{m}$.



(a)



(b)

Figure 9: Finite element results for *small pores* microstructures: (a) typical high-strain-energy sample (98% of cases), and (b) anomalous low-strain-energy sample, showing the microstructure indicator function $\phi(\mathbf{x})$, the magnitude of displacement $\|\mathbf{u}\|$, and components of Cauchy stress \mathbf{T} .

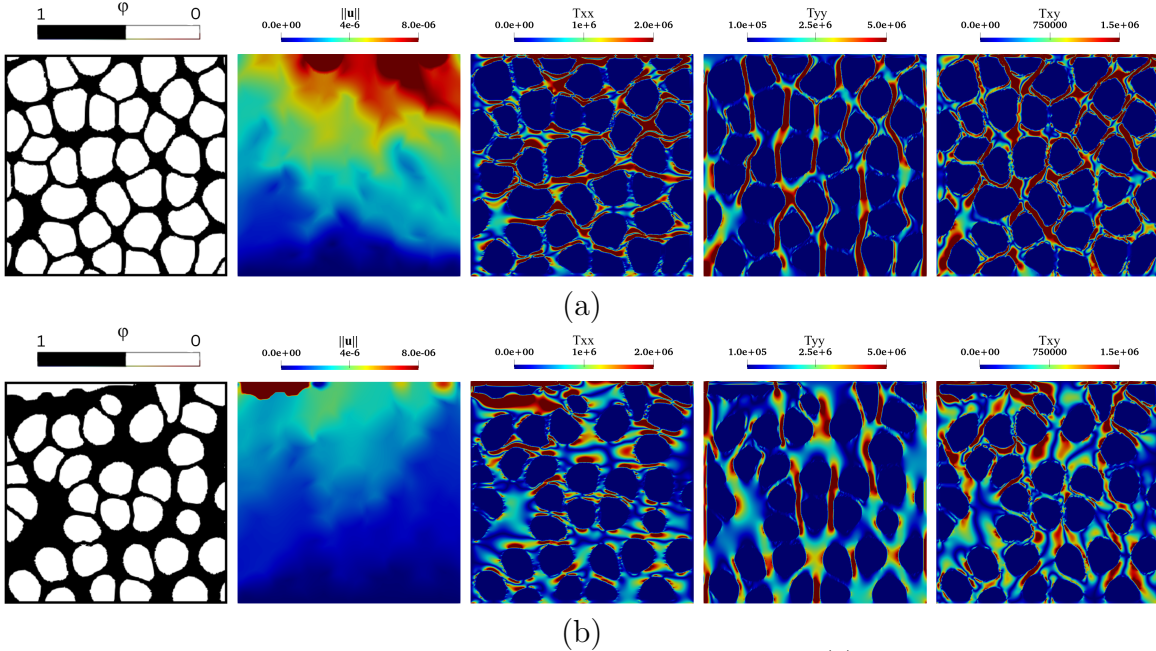


Figure 10: Finite element results for *medium pores* microstructures: (a) typical high-strain-energy sample (97% of cases), and (b) anomalous low-strain-energy sample, showing the microstructure indicator function $\phi(\mathbf{x})$, the magnitude of displacement $\|\mathbf{u}\|$, and components of Cauchy stress \mathbf{T} .

with an average pore size of $12 \mu\text{m}$ (intermediate between *small pores* and *medium pores*) and 10 with an average pore size of $22 \mu\text{m}$ (between *medium pores* and *large pores*). The FSLBM parameters matched those used for training data generation, except for the average pore size and initial bubble count: 75 bubbles for the $12 \mu\text{m}$ microstructures and 35 for the $22 \mu\text{m}$ cases.

The bimodal distribution of strain energy probabilities, illustrated in Figure 8(d), reflects the distinct mechanical behaviors exhibited within and across the three categories of ceramic aerogel microstructures. Representative FE solutions for these categories are presented in Figures 9–11. For the *small pores* category, the majority of microstructural samples (approximately 98%) exhibit strain energies ranging from 1000×10^{-7} to 1100×10^{-7} mJ with occasional anomalies at lower strain energy levels. As shown in Figure 9, most microstructures demonstrate mechanical deformation dominated by high-strain pathways connecting the top and bottom boundaries. In some cases, these pathways are interrupted by isolated solid-phase regions, leading to deviations in mechanical response. A similar trend is observed for the *medium pores* category, where strain energies predominantly range from 1150×10^{-7} to 1300×10^{-7} mJ, with sporadic anomalies indicating increased mechanical strength (Figure 10). In contrast, the *large pores* category exhibits a distinct mechanical behavior characterized by a near-normal strain energy distribution ranging from 800×10^{-7} to 1300×10^{-7} mJ (Figure 11). These variations highlight the strong influence of pore size and distribution on the mechanical properties of ceramic aerogels.

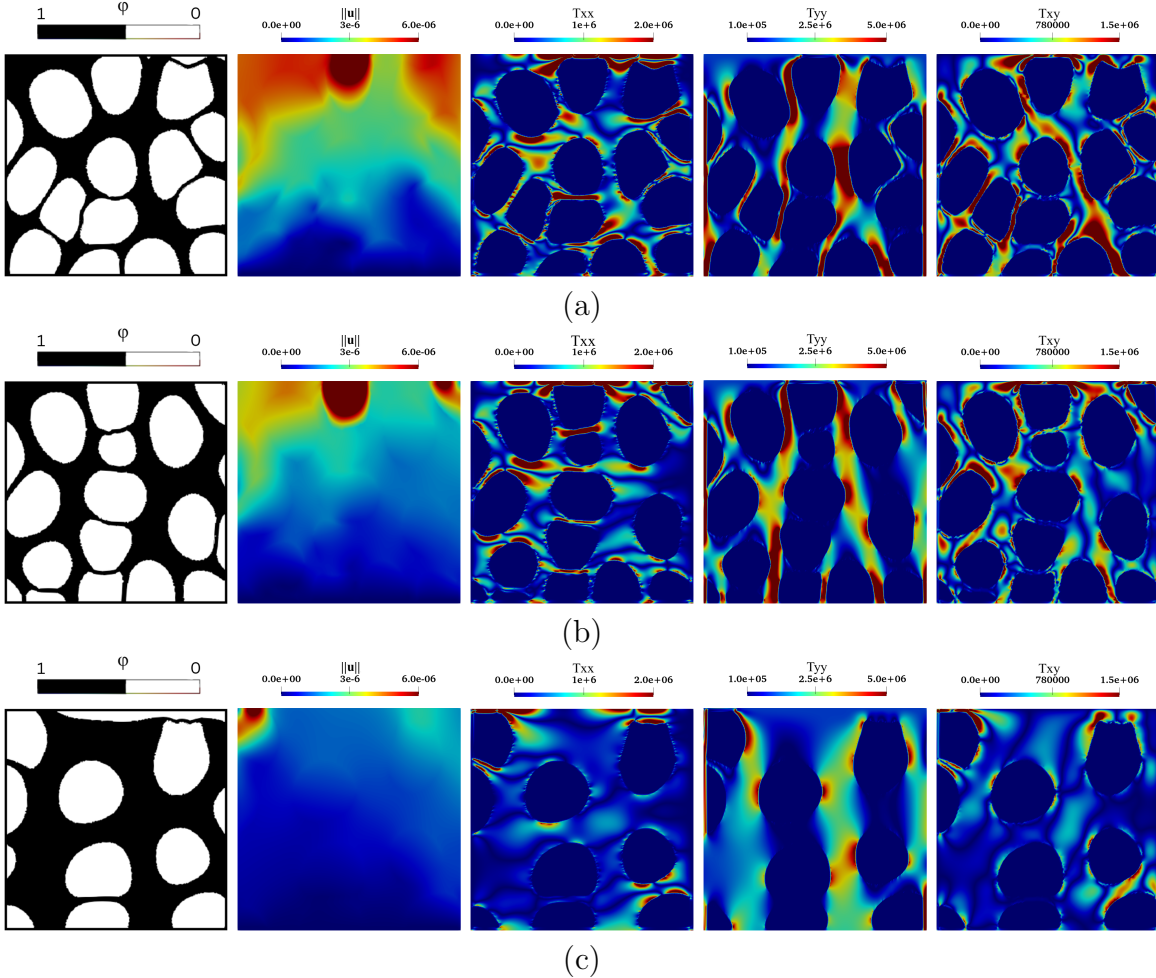


Figure 11: Finite element results for *large pores* microstructures: (a) low-strain-energy sample (25% of cases), and (b) medium-strain-energy sample (25% of cases), and (c) high-strain-energy sample (25% of cases), showing the microstructure indicator function $\phi(\mathbf{x})$, the magnitude of displacement $\|\mathbf{u}\|$, and components of Cauchy stress \mathbf{T} .

Network architecture and training. The BayesCNN’s architecture and hyperparameters were determined through a systematic validation process using the in-distribution dataset (10% of high-fidelity data generated using stochastic FE model). Table A.2 (see Appendix) details the architecture, including input and output shapes and the total number of parameters. Key hyperparameters for the variational inference include the learning rate employed by the Adam optimizer and β in (23), which balances data misfit and prior regularization in the Bayesian framework.

Figure 12 illustrates the process of selecting these hyperparameters. The validation loss, defined as the mean squared error between validation data and the corresponding BayesCNN mean predictions, is plotted over training epochs for four different learning rates in Figure 12(a). The four learning rates yield similar validation losses over the chosen course of epochs. A learning rate of 0.002, yielding the most stable validation loss decrease (fewest number of spikes), was chosen for Bayesian training. Addition-

ally, the validation loss stopped decreasing around 400 epochs, corresponding to the minimum loss. The accuracy of Bayesian inference depends critically on the proper selection of β . Overestimating β diminishes the influence of valuable data, while underestimating it leads to over-fitting, biased parameter estimates. To avoid such biases, β was tuned based on its impact on R^2 values computed as,

$$R^2 = 1 - \frac{\sum_{j=1}^{N_{id}} (Q_j^{FE} - \mathbb{E}(Q^{CNN}))^2}{\sum_{j=1}^{N_{id}} (Q_j^{FE} - \mathbb{E}(Q^{FE}))^2}, \quad (24)$$

where N_{id} is the number of in-distribution datapoints, Q^{FE} is the deterministic strain energy computed from FE model for each microstructure sample, and Q^{CNN} the BayesCNN prediction computed using 40 samples of the weight parameters for each microstructure. As shown in Figure 12(b), $\beta = 0.01$ consistently achieves the highest R^2 for both in-distribution and out-of-distribution data, and thus selected for the Bayesian inference. This result also aligns with the cold posterior effect [47], demonstrating improved predictive performance for β below 1.

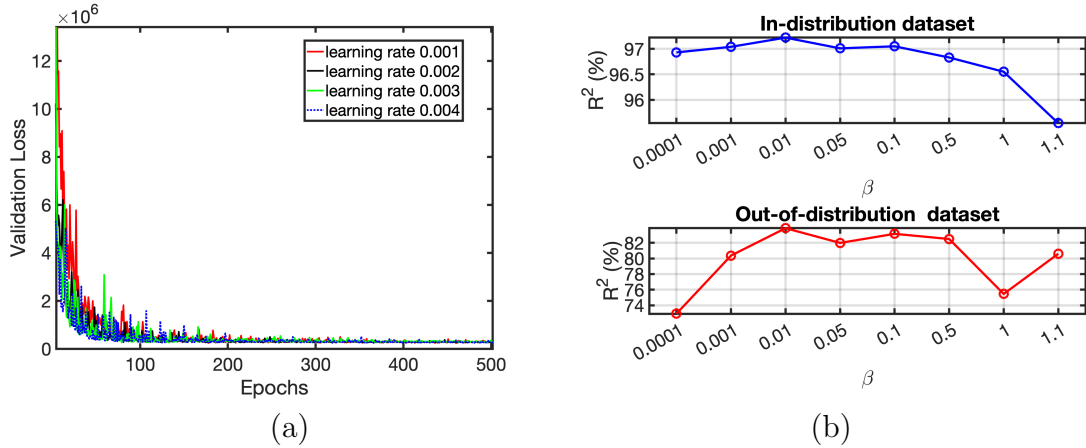


Figure 12: Hyperparameter selection for Bayesian inference: (a) Validation loss as a function of training epochs for various learning rates used in the optimizer. (b) Comparison of R^2 values across different β values in both in-distribution and out-of-distribution datasets.

BayesCNN prediction. Figures 13–15 show the in-distribution prediction results of the BayesCNN model for the *small pores*, *medium pores*, and *large pores* microstructure classes. Each figure includes the probability distribution of high-fidelity strain energy data for the corresponding class and the three representative microstructure samples including the true strain energy value from the FE model, $Q^{FE} = \mathcal{F}_{FE}(\varphi, \boldsymbol{\theta}_{FE})$ and the BayesCNN-predicted probability distribution, $Q^{CNN} = \mathcal{G}_{CNN}(\varphi, \boldsymbol{w}_{CNN})$, obtained using 40 samples of weight parameters \boldsymbol{w}_{CNN} . In all cases, the true values consistently fall within the BayesCNN-predicted distributions, demonstrating the model’s reliability for in-distribution predictions.

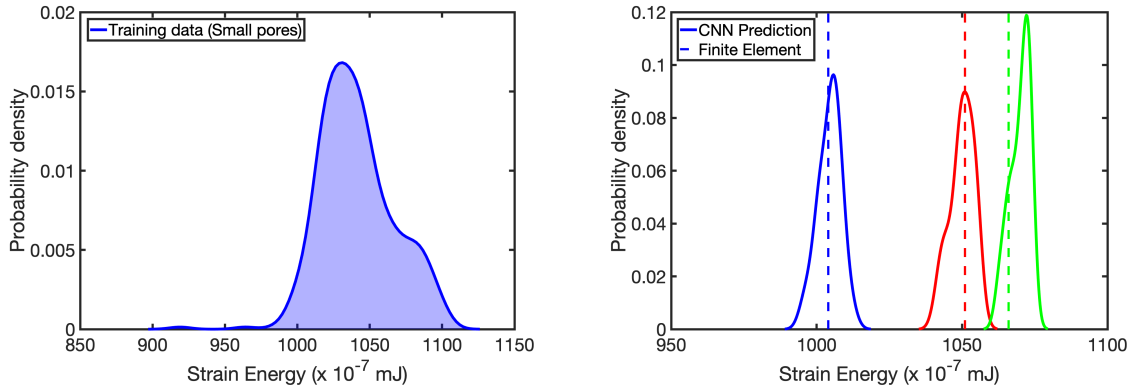


Figure 13: *Small pores* microstructures (pore size = $6\mu\text{m}$): Training dataset (top left) and in-distribution predictions of the BayesCNN for three microstructures.

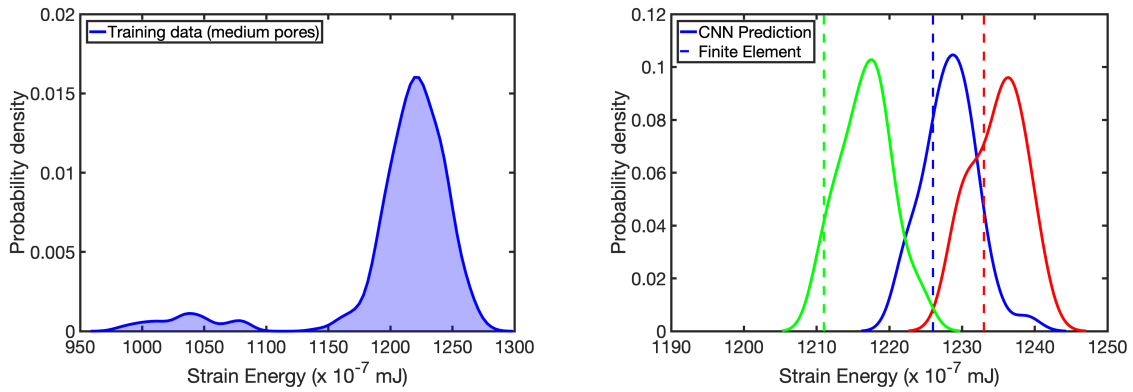


Figure 14: *Medium pores* microstructures (pore size= $18\mu\text{m}$): Training dataset (top left) and in-distribution predictions of the BayesCNN for three microstructures.

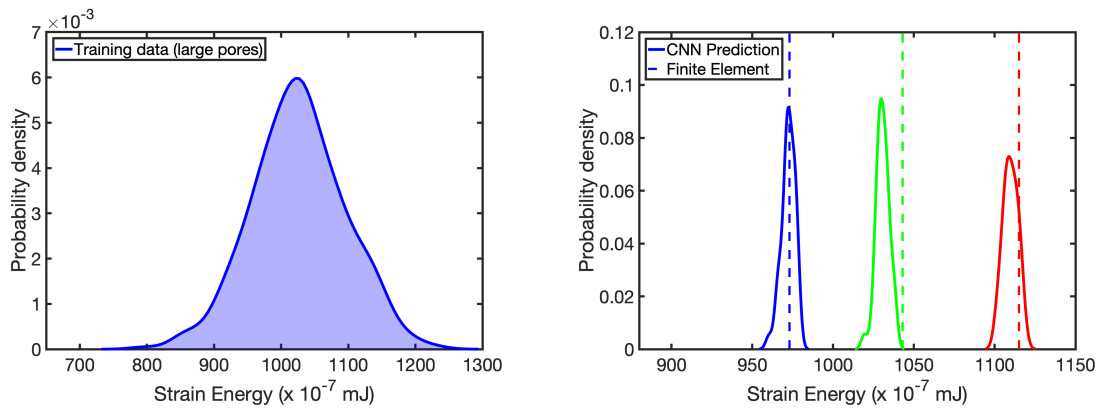


Figure 15: *Large pores* microstructures (pore size = $25\mu\text{m}$): Training dataset (top left) and in-distribution predictions of the BayesCNN for three microstructures.

A key advantage of deep learning surrogate models for microstructure-property mapping in materials design and engineering lies in their accuracy and reliability for

out-of-distribution predictions. This refers to the model’s ability to generalize to new microstructural features beyond the classes represented in the training data. Figure 16 compares the true strain energy, $Q^{FE} = \mathcal{F}_{FE}(\varphi, \boldsymbol{\theta}_{FE})$, computed via the FE model, with the probability distribution of strain energy predicted by the BayesCNN surrogate model, $Q^{CNN} = \mathcal{G}_{CNN}(\varphi, \boldsymbol{w}_{CNN})$, for a few samples.

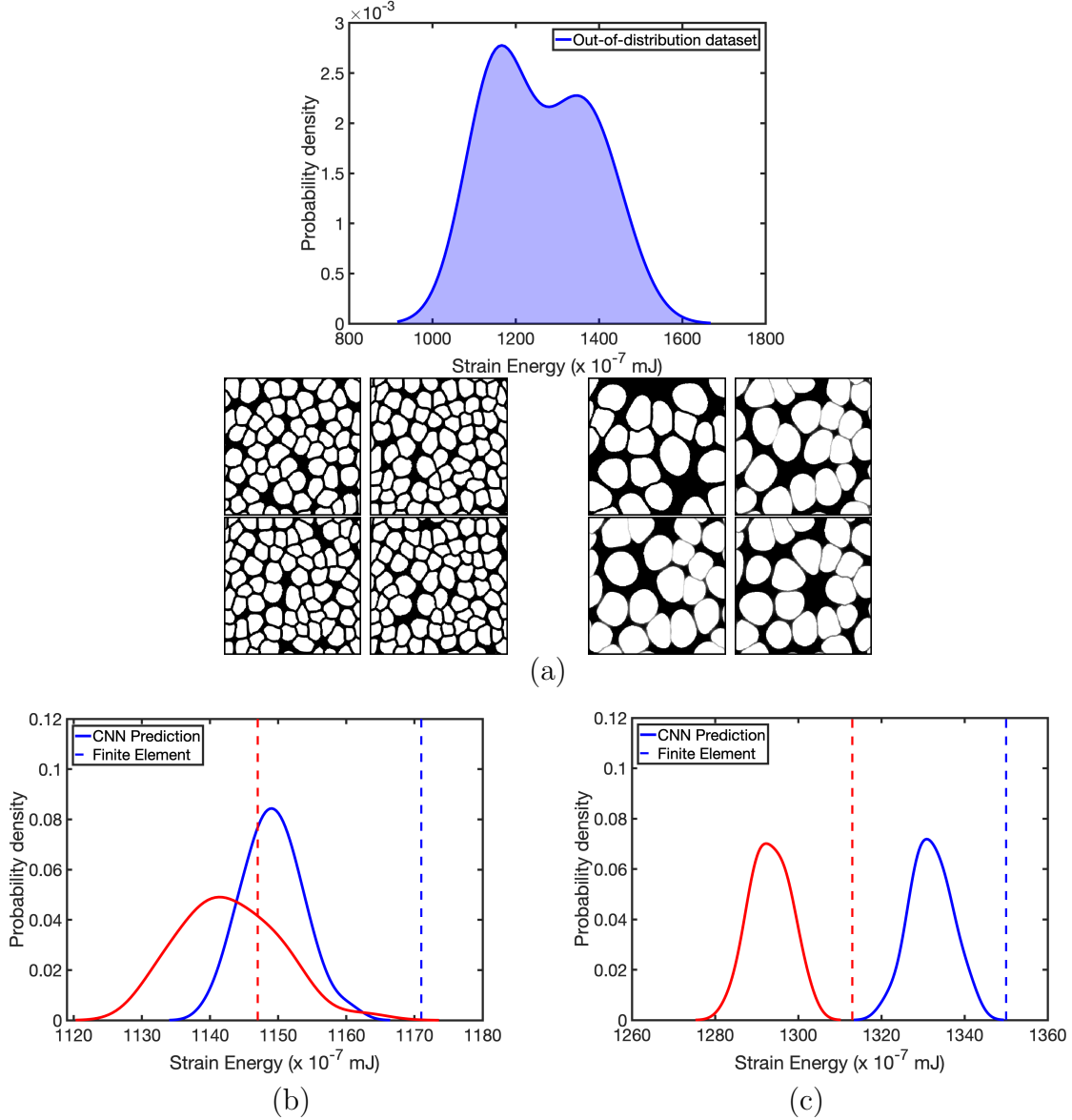


Figure 16: Out-of-distribution predictions of the BayesCNN model: (a) Microstructure samples with average pore sizes of 12 μm (between *small pores* and *medium pores*) and 22 μm (between *medium pores* and *large pores*), along with the strain energy probability distribution of out-of-distribution dataset. (b) BayesCNN predictions for two microstructures with 12 μm pores. (c) BayesCNN predictions for two microstructures with 22 μm pores.

The accuracy and reliability of the BayesCNN predictions are further evaluated for

both in-distribution and out-of-distribution dataset in Figure 17. In this figure, the *prediction error* is defined as $|\mathbb{E}[Q^{CNN}] - Q^{FE}|$, and the *uncertainty* is represented by the variance of the BayesCNN predictions, $\mathbb{V}[Q^{CNN}]$. These results indicate that the BayesCNN model successfully identifies out-of-distribution data, as reflected by lower accuracy and reliability in its predictions for such cases. The model performs well in interpolating between *small pores* and *medium pores* microstructures. However, its accuracy diminishes for out-of-distribution data with an average pore size of $22 \mu\text{m}$, representing microstructures between *medium pores* and *large pores*.

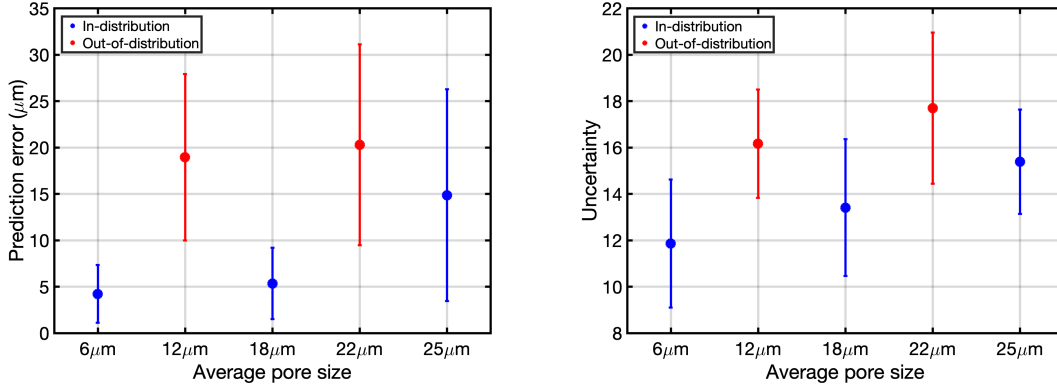


Figure 17: The BayesCNN model’s prediction accuracy and reliability for in-distribution and out-of-distribution datasets using 10 samples. The *prediction error* is defined as $|\mathbb{E}[Q^{CNN}] - Q^{FE}|$, and the *uncertainty* is defined as $\mathbb{V}[Q^{CNN}]$.

5. Conclusions

This study introduces an integrated deep learning surrogate modeling framework for efficient uncertainty propagation across the synthesis, microstructure, and properties of ceramic aerogel porous materials. The stochastic microstructure surrogate employs a scalable Wasserstein Generative Adversarial Network with Gradient Penalty (WGAN-GP) to generate ensembles of morphologically consistent microstructures over arbitrarily large domains, trained on smaller domain size samples from Lattice Boltzmann simulations of the foaming process. For property prediction, a Bayesian Convolutional Neural Network (BayesCNN) is developed to estimate weight parameter distributions using small, uncertain high-fidelity datasets from finite element elasticity simulations. Numerical results demonstrate that the WGAN-GP effectively generates microstructures consistent with the morphology of training data (in terms of pore size distribution and two-point correlation) across larger domains. The BayesCNN accurately maps microstructural images to strain energy while quantifying uncertainty, achieving reliable predictions for unseen in-distribution data. However, its predictive accuracy and confidence decline for out-of-distribution microstructures with morphologically distinct attributes. Notably, while the model performs well in interpolating between small and medium pore sizes, it struggles with medium-to-large pore sizes due to significant differences in the deformation mechanisms of aerogels with larger pores.

Future work will focus on enhancing the framework by incorporating aerogel synthesis parameters as additional inputs to the WGAN-GP, enabling the discovery of novel morphologies that interpolate between training data for specific synthesis parameter combinations, as demonstrated in [37]. The BayesCNN will be further evaluated across a wider range of aerogel microstructures, investigating both interpolation and extrapolation capabilities. This includes assessing predictive accuracy for microstructures with diverse pore size distributions and integrating nonlinear finite element models based on continuum damage mechanics to capture complex deformation behaviors of ceramic aerogels. Additionally, the surrogate model will be refined through improved architecture design and hyperparameter selection using a hierarchical Bayesian inference framework [18]. This approach will identify the most plausible BayesCNN model under constraints of limited and uncertain training data, enhancing the framework reliable deployment in high-consequence material discovery scenarios.

This study tackles the computational challenges of model-driven materials discovery by developing a validated deep learning surrogate model for synthesis-microstructure-property relationships using limited and uncertain high-fidelity data. It also paves the way for advancing predictive accuracy and confidence in data-driven surrogate modeling for physical and engineering systems.

Acknowledgments

MAI and DF extend their gratitude for the financial support of this work from the Research Foundation of The State University of New York (SUNY) under grant number 1191358. Additionally, the authors would like to acknowledge the support provided by the Center for Computational Research at the University at Buffalo.

Appendix A. Appendix: Deep learning architectures

Layer	Type	Kernel	Stride	Input Shape	Output Shape	Parameters
Input	-	-	-	$3 \times 168 \times 168$	$3 \times 168 \times 168$	0
Conv1	BBBConv2d	5×5	1×1	$3 \times 168 \times 168$	$6 \times 164 \times 164$	456
Act1	Softplus	-	-	$6 \times 164 \times 164$	$6 \times 164 \times 164$	0
Pool1	MaxPool	2×2	2×2	$6 \times 164 \times 164$	$6 \times 82 \times 82$	0
Conv2	BBBConv2d	5×5	1×1	$6 \times 82 \times 82$	$16 \times 78 \times 78$	2,416
Act2	Softplus	-	-	$16 \times 78 \times 78$	$16 \times 78 \times 78$	0
Pool2	MaxPool	2×2	2×2	$16 \times 78 \times 78$	$16 \times 39 \times 39$	0
Flatten	Flatten	-	-	$16 \times 39 \times 39$	24,336	0
FC1	BBBLinear	-	-	24,336	120	2,920,440
Act3	Softplus	-	-	120	120	0
FC2	BBBLinear	-	-	120	84	10,164
Act4	Softplus	-	-	84	84	0
Regression	BBBLinear	-	-	84	1	85

Table A.2: Architecture of the BayesCNN model and total number of parameters.

Layer	Dimension	Kernel	Stride	Padding	Batch Normalization	Activation Function
Generator						
Layer 1	$-1 \times 8 \times 8 \times 512$	4×4	2×2	1×1	Yes	ReLU
Layer 2	$-1 \times 16 \times 16 \times 256$	4×4	2×2	1×1	Yes	ReLU
Layer 3	$-1 \times 32 \times 32 \times 128$	4×4	2×2	1×1	Yes	ReLU
Layer 4	$-1 \times 64 \times 64 \times 64$	4×4	2×2	1×1	Yes	ReLU
Layer 5	$-1 \times 128 \times 128 \times 1$	4×4	2×2	1×1	No	Tanh
Discriminator						
Layer 1	$-1 \times 64 \times 64 \times 64$	4×4	2×2	1×1	Yes	LeakyReLU
Layer 2	$-1 \times 32 \times 32 \times 128$	4×4	2×2	1×1	Yes	LeakyReLU
Layer 3	$-1 \times 16 \times 16 \times 256$	4×4	2×2	1×1	Yes	LeakyReLU
Layer 4	$-1 \times 8 \times 8 \times 512$	4×4	2×2	1×1	Yes	LeakyReLU
Layer 5	$-1 \times 1 \times 1 \times 1$	4×4	2×2	1×1	No	-

Table A.1: Architecture of WGAN-GP with the output dimension from each layer.

Bibliography

- [1] N. Hazarika, M. A. Irfan, Aerogel-a future material for aircraft structure, International Journal and Magazine of Engineering, Technology, Management and Research 3 (2016).
- [2] J. Fesmire, Aerogels insulate against extreme temperatures, NASA Spinoffs (01 2010).
- [3] L. An, B. Liang, Z. Guo, J. Wang, C. Zhou, C. Li, Y. Huang, Y. Hu, Z. Li, J. Armstrong, D. Faghihi, S. Ren, Wearable aramid-ceramic aerogel composite for harsh environment, Advanced Engineering Materials (submitted).
- [4] X. Wang, G. Li, G. Hong, Q. Guo, X. Zhang, Graphene aerogel templated fabrication of phase change microspheres as thermal buffers in microelectronic devices, ACS applied materials & interfaces 9 (47) (2017) 41323–41331.
- [5] H. Choi, T. Kim, T. Kim, S. Moon, S. Yoo, V. G. Parale, R. P. Dhavale, K. Kang, H. Sohn, H.-H. Park, Ultralow dielectric cross-linked silica aerogel nanocomposite films for interconnect technology, Applied Materials Today 28 (2022) 101536.
- [6] J. Tan, P. Maleki, L. An, M. Di Luigi, U. Villa, C. Zhou, S. Ren, D. Faghihi, A predictive multiphase model of silica aerogels for building envelope insulations, Computational Mechanics 69 (6) (2022) 1457–1479.
- [7] A. Acharya, D. Joshi, V. A. Gokhale, Aerogel—a promising building material for sustainable buildings, Chemical and Process Engineering Research 9 (2013) 1–6.

- [8] K. Rajan, Informatics for materials science and engineering: data-driven discovery for accelerated experimentation and application, Butterworth-Heinemann, 2013.
- [9] N. R. Council, D. on Engineering, P. Sciences, N. M. A. Board, C. on Integrated Computational Materials Engineering, Integrated computational materials engineering: a transformational discipline for improved competitiveness and national security, National Academies Press, 2008.
- [10] B. Xu, H. Yin, X. Jiang, C. Zhang, R. Zhang, Y. Wang, X. Qu, Computational materials design: Composition optimization to develop novel ni-based single crystal superalloys, Computational Materials Science 202 (2022) 111021.
- [11] S. Zeng, et al., Atom table convolutional neural networks for an accurate prediction of compounds properties. 5, 84 (2019).
- [12] K. Choudhary, B. DeCost, C. Chen, A. Jain, F. Tavazza, R. Cohn, C. W. Park, A. Choudhary, A. Agrawal, S. J. Billinge, et al., Recent advances and applications of deep learning methods in materials science, npj Computational Materials 8 (1) (2022) 59.
- [13] G. Xiong, C. Wang, Y. Yan, L. Zhang, Y. Su, Indexing high-noise electron backscatter diffraction patterns using convolutional neural network and transfer learning, Computational Materials Science 233 (2024) 112718.
- [14] J. Zhang, L. Zhang, Y. Sun, W. Li, R. Quhe, Named entity recognition in the perovskite field based on convolutional neural networks and matbert, Computational Materials Science 240 (2024) 113014.
- [15] M. Qian, J. Zhou, J. Wang, L. Ruan, Z. Xiang, X. Hu, Permeability prediction of complex porous materials by conjugating generative adversarial and convolutional neural networks, Computational Materials Science 238 (2024) 112942.
- [16] R. M. Neal, Bayesian learning for neural networks, Vol. 118, Springer Science & Business Media, 2012.
- [17] C. Blundell, J. Cornebise, K. Kavukcuoglu, D. Wierstra, Weight uncertainty in neural network, in: International conference on machine learning, PMLR, 2015, pp. 1613–1622.
- [18] P. K. Singh, K. A. Farrell-Maupin, D. Faghihi, A framework for strategic discovery of credible neural network surrogate models under uncertainty, Computer Methods in Applied Mechanics and Engineering. (arXiv preprint arXiv:2403.08901) (in press).
- [19] A. Olivier, M. D. Shields, L. Graham-Brady, Bayesian neural networks for uncertainty quantification in data-driven materials modeling, Computer methods in applied mechanics and engineering 386 (2021) 114079.

- [20] Y. Zhu, N. Zabaras, Bayesian deep convolutional encoder–decoder networks for surrogate modeling and uncertainty quantification, *Journal of Computational Physics* 366 (2018) 415–447.
- [21] K. Shridhar, F. Laumann, M. Liwicki, A comprehensive guide to bayesian convolutional neural network with variational inference, arXiv preprint arXiv:1901.02731 (2019).
- [22] R. Yang, F. Hu, L. An, J. Armstrong, Y. Hu, C. Li, Y. Huang, S. Ren, A hierarchical mesoporous insulation ceramic, *Nano Letters* 20 (2) (2019) 1110–1116.
- [23] K. N. Kyzyurova, J. O. Berger, R. L. Wolpert, Coupling computer models through linking their statistical emulators, *SIAM/ASA Journal on Uncertainty Quantification* 6 (3) (2018) 1151–1171.
- [24] A. S. Dorcheh, M. Abbasi, Silica aerogel; synthesis, properties and characterization, *Journal of materials processing technology* 199 (1-3) (2008) 10–26.
- [25] J. Wang, D. Petit, S. Ren, Transparent thermal insulation silica aerogels, *Nanoscale Advances* 2 (12) (2020) 5504–5515.
- [26] C. Körner, M. Thies, R. F. Singer, Modeling of metal foaming with lattice boltzmann automata, *Advanced Engineering Materials* 4 (10) (2002) 765–769.
- [27] C. Körner, M. Thies, T. Hofmann, N. Thürey, U. Rüde, Lattice boltzmann model for free surface flow for modeling foaming, *Journal of Statistical Physics* 121 (1-2) (2005) 179–196.
- [28] D. Anderl, S. Bogner, C. Rauh, U. Rüde, A. Delgado, Free surface lattice boltzmann with enhanced bubble model, *Computers & Mathematics with Applications* 67 (2) (2014) 331–339.
- [29] S. Donath, C. Feichtinger, T. Pohl, J. Götz, U. Rüde, Localized parallel algorithm for bubble coalescence in free surface lattice-boltzmann method, in: *European Conference on Parallel Processing*, Springer, 2009, pp. 735–746.
- [30] M. Ataei, V. Shaayegan, F. Costa, S. Han, C. Park, M. Bussmann, Lbfoam: An open-source software package for the simulation of foaming using the lattice boltzmann method, *Computer Physics Communications* (2020) 107698.
- [31] J. Latt, O. Malaspinas, D. Kontaxakis, A. Parmigiani, D. Lagrava, F. Brogi, M. B. Belgacem, Y. Thorimbert, S. Leclaire, S. Li, F. Marson, J. Lemus, C. Kotsalos, R. Conradin, C. Coreixas, R. Petkantchin, F. Raynaud, J. Beny, B. Chopard, Palabos: Parallel lattice boltzmann solver, *Computers & Mathematics with Applications* (2020).

- [32] S. Chen, G. D. Doolen, Lattice boltzmann method for fluid flows, *Annual review of fluid mechanics* 30 (1) (1998) 329–364.
- [33] M. Do-Quang, E. Aurell, M. Vergassola, An inventory of lattice boltzmann models of multiphase flows, *Parallel and Scientific Computing*, Report 00 3 (2000).
- [34] J. Boyd, J. M. Buick, S. Green, Analysis of the casson and carreau-yasuda non-newtonian blood models in steady and oscillatory flows using the lattice boltzmann method, *Physics of Fluids* 19 (9) (2007) 093103.
- [35] R. Bridson, Fast poisson disk sampling in arbitrary dimensions., *SIGGRAPH sketches* 10 (1) (2007) 1.
- [36] I. Goodfellow, J. Pouget-Abadie, M. Mirza, B. Xu, D. Warde-Farley, S. Ozair, A. Courville, Y. Bengio, Generative adversarial nets, in: *Advances in neural information processing systems*, 2014, pp. 2672–2680.
- [37] S. Chun, S. Roy, Y. T. Nguyen, J. B. Choi, H. S. Udaykumar, S. S. Baek, Deep learning for synthetic microstructure generation in a materials-by-design framework for heterogeneous energetic materials, *Scientific reports* 10 (1) (2020) 13307.
- [38] C. Chen, X. Han, Y. Zhang, P. K. Liaw, J. Ren, Phase prediction of high-entropy alloys based on machine learning and an improved information fusion approach, *Computational Materials Science* 239 (2024) 112976. doi:<https://doi.org/10.1016/j.commatsci.2024.112976>.
URL <https://www.sciencedirect.com/science/article/pii/S0927025624001976>
- [39] O. Schenk, M. Becker, Y. Deng, P. Niemietz, T. Bergs, C. Broeckmann, Prediction of the microstructure of cold-compacted astaloy 85mo with deep generative models, *Computational Materials Science* 242 (2024) 113064. doi:<https://doi.org/10.1016/j.commatsci.2024.113064>.
URL <https://www.sciencedirect.com/science/article/pii/S0927025624002854>
- [40] Y. Fukatsu, T.-T. Chen, T. Ogawa, F. Sun, Y. Adachi, Y. Tanaka, S. Ishikawa, Analysis of the strength–ductility balance of dual-phase steel using a combination of generative adversarial networks and finite element method, *Computational Materials Science* 243 (2024) 113143. doi:<https://doi.org/10.1016/j.commatsci.2024.113143>.
URL <https://www.sciencedirect.com/science/article/pii/S0927025624003641>
- [41] M. Qian, J. Zhou, J. Wang, L. Ruan, Z. Xiang, X. Hu, Permeability prediction of complex porous materials by conjugating generative adversarial and convolutional neural networks, *Computational Materials Science* 238 (2024) 112942.

doi:<https://doi.org/10.1016/j.commatsci.2024.112942>.

URL <https://www.sciencedirect.com/science/article/pii/S0927025624001630>

- [42] I. Gulrajani, F. Ahmed, M. Arjovsky, V. Dumoulin, A. C. Courville, Improved training of wasserstein gans, *Advances in neural information processing systems* 30 (2017).
- [43] L. Yang, D. Zhang, G. E. Karniadakis, Physics-informed generative adversarial networks for stochastic differential equations, *SIAM Journal on Scientific Computing* 42 (1) (2020) A292–A317.
- [44] I. A. Baratta, J. P. Dean, J. S. Dokken, M. Habera, J. S. Hale, C. N. Richardson, M. E. Rognes, M. W. Scroggs, N. Sime, G. N. Wells, DOLFINx: The next generation FEniCS problem solving environment (Dec. 2023). doi:10.5281/zenodo.10447666.
URL <https://doi.org/10.5281/zenodo.10447666>
- [45] S. Bhattacharjee, Integrating scientific machine learning and physics-based models for quantification of uncertainty in thermal properties of silica aerogel, Master's thesis, State University of New York at Buffalo (2023).
- [46] R. Bostanabad, Y. Zhang, X. Li, T. Kearney, L. C. Brinson, D. W. Apley, W. K. Liu, W. Chen, Computational microstructure characterization and reconstruction: Review of the state-of-the-art techniques, *Progress in Materials Science* 95 (2018) 1–41.
- [47] F. Wenzel, K. Roth, B. S. Veeling, J. Swiatkowski, L. Tran, S. Mandt, J. Snoek, T. Salimans, R. Jenatton, S. Nowozin, How good is the bayes posterior in deep neural networks really?, *arXiv preprint arXiv:2002.02405* (2020).